

# Moiré flat bands in alternating twisted MoTe<sub>2</sub> multilayer

Miao Liang,<sup>1</sup> Shi-Ping Ding,<sup>1</sup> Ming Wu,<sup>1</sup> Chen Zhao,<sup>1</sup> and Jin-Hua Gao<sup>1,\*</sup>

<sup>1</sup>*School of Physics and Wuhan National High Magnetic Field Center, Huazhong University of Science and Technology, Wuhan 430074, China*

The long-awaited fractional quantum anomalous Hall (FQAH) effect recently has been observed in the twisted MoTe<sub>2</sub> homobilayers, causing a great sensation. Here, we theoretically investigate the moiré band structures of a closely related system, the alternating twisted multilayer MoTe<sub>2</sub> (ATML-MoTe<sub>2</sub>), where the adjacent layers have opposite twist angles. We illustrate that such ATML-MoTe<sub>2</sub> is a very unique moiré system, exhibiting multiple topological flat bands highly controllable by the layer number and twist angle, which is not only an ideal platform to simulate Hubbard model, but also may host FQAH states. Specifically, an  $N$ -layer ATML-MoTe<sub>2</sub> ( $N \geq 3$ ) always possesses  $N - 2$  topological flat bands near Fermi energy  $E_f$ , which has an odd-even dependent decomposition rule to understand the behaviors of the moiré flat bands. We predict three intriguing examples: (1) The AT3L-MoTe<sub>2</sub> ( $N = 3$ ) has one isolated moiré flat band, which corresponds to a triangular lattice Hubbard model, resembling the twisted TMD heterobilayers. (2) The AT4L-MoTe<sub>2</sub> ( $N = 4$ ) has two topological flat bands that are very similar to the twisted MoTe<sub>2</sub> homobilayers, implying the possible existence of FQAH states. (3) When  $N > 4$ , the giant density of states (DOS) induced by the multiple moiré flat bands may induce exotic correlated states.

## I. INTRODUCTION

Recently, the fractional quantum anomalous Hall (FQAH) effect has been successfully observed in twisted MoTe<sub>2</sub> homobilayers, which has sparked widespread research interest<sup>1-5</sup>. The emergence of the FQAH states in twisted MoTe<sub>2</sub> homobilayers is attributed to its isolated topological moiré flat band<sup>6-16</sup>. Meanwhile, it is further suggested that the uniformly distributed Berry curvature is crucial for the topological flat bands to realize the FQAH states<sup>17</sup>. All of these important theoretical and experimental studies reveal the uniqueness of the MoTe<sub>2</sub>-based moiré structures.

The alternating twisted multilayer moiré structure is a natural generalization of the twisted homobilayers, where the twist angles of adjacent layers are  $\pm\theta$  with opposite rotation directions. The celebrated example is the alternating twisted few-layer graphene (ATFLG)<sup>18-32</sup>, which also host moiré flat bands very similar as the twisted bilayer graphene (TBG)<sup>33-37</sup>. Interestingly, it is proved that there is a decomposition rule, by which an ATFLG can be decomposed into several effective TBGs with renormalized parameters<sup>18</sup>. Therefore, it can be expected that correlated states in TBG will also exist in ATFLG. Note that superconductivity in ATFLG has been observed in recent experiments<sup>23,24,38-40</sup>. Inspired by the success of ATFLG, a fascinating question arises: can the alternating twisted multilayer MoTe<sub>2</sub> (ATML-MoTe<sub>2</sub>) generate richer moiré band structures, and thus induce more novel correlation and topological effects, such as FQAH states?

In this work, we systematically study the moiré band structures of the ATML-MoTe<sub>2</sub> based on the continuum model method. We find that ATML-MoTe<sub>2</sub> is a unique moiré system hosting multiple topological flat bands, which are highly adjustable by the layer number and twist angle. Specifically, an  $N$ -layer ATML-MoTe<sub>2</sub> ( $N \geq 3$ ) always has  $N - 2$  topological flat bands at small

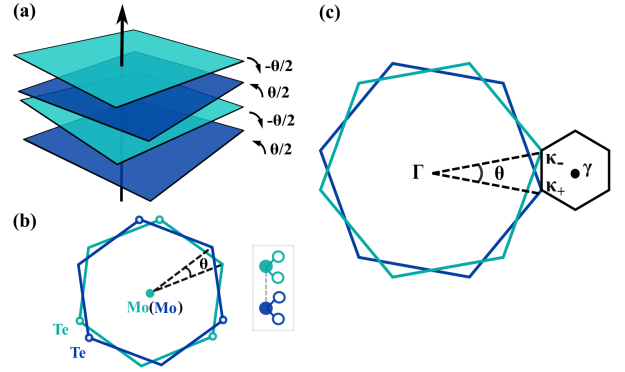


FIG. 1. Schematic diagram of ATML-MoTe<sub>2</sub>. (a) Schematic of AT4L-MoTe<sub>2</sub>, with the rotation directions of the 1st and 3rd layers (blue) opposite to those of the 2nd and 4th layers (green). (b) Top view of an AA-stacked AT4L-MoTe<sub>2</sub>. The inset shows a side view between adjacent layers. (c) Brillouin zones of the odd-layer (blue), the even-layer (green), and the moiré Brillouin zone (black).

twist angle, and the intriguing features of these topological flat bands are summarized as follows:

1. *Multiple degenerate flat bands at small twist angle.* When  $\theta \lesssim 1.4^\circ$ , the  $N - 2$  flat bands of the  $N$ -layer ATML-MoTe<sub>2</sub> are nearly degenerate at  $E_f$ , with a large band gap separating these flat bands from other low energy bands.
2. *Isolated topological flat band at magic angle.* As  $\theta$  increases, the degeneracy of these flat bands is lifted and an isolated flat band appears near the  $E_f$ . For even  $N$ , there is a magic angle near  $2.02^\circ$ , at which an isolated topological flat band is achieved.
3. *Decomposition rules.* An even-odd dependent decomposition rule is proved, which can well interpret the origin and behaviors of the  $N - 2$  topological

flat bands. Meanwhile, there exists a mirror symmetry decomposition for the odd  $N$  cases.

Based on our calculation, we can give three interesting predictions:

1. The AT3L-MoTe<sub>2</sub> ( $N = 3$ ) has one isolated moiré flat band near  $E_f$ , which can be described as a triangular lattice Hubbard model, resembling the twisted transition metal dichalcogenides (TMD) heterobilayers<sup>41-43</sup>.
2. The AT4L-MoTe<sub>2</sub> ( $N = 4$ ) has two topological moiré flat bands near  $E_f$ , which exhibit similar properties to those of the twisted MoTe<sub>2</sub> homobilayers, making it a promising moiré system for achieving the FQAH effect.
3. When  $N > 4$ , the presence of multiple degenerate flat bands implies a giant DOS at  $E_f$ , which is expected to promote the formation of various correlated insulating states.

Our results indicate that the ATML-MoTe<sub>2</sub> is an ideal platform for simulating both the Hubbard model and FQAH states, promising to host a variety of exotic topological and correlated quantum states like that in twisted TMD homobilayers<sup>1-3,5-17,44-52</sup>. We expect that our predictions can be immediately tested in future experiments.

The paper is organized as follows. In Sec. II, the model and methods of ATML-MoTe<sub>2</sub> used in the calculations are given. In Sec. III, we discuss the calculation results. Sec. IV is a short summary.

## II. MODEL AND METHODS

### A. The continuum model of ATML-MoTe<sub>2</sub>

In Fig. 1, we give a schematic of ATML-MoTe<sub>2</sub>. The continuum model of ATML-MoTe<sub>2</sub> can be given in a similar way to that of the twisted TMD homobilayers<sup>6</sup>. For each MoTe<sub>2</sub> monolayer, the valence electrons are around the  $\pm K$  valleys, which are mainly of the  $d$ -orbital character with opposite spin due to spin-valley locking<sup>6,53</sup>. Considering the layer-dependent potential and interlayer tunneling, the Hamiltonian of  $N$ -layer ATML-MoTe<sub>2</sub> of the  $+K$  valley is

$$\mathcal{H} = \begin{pmatrix} \mathcal{H}_1 & T_{bm} & 0 \\ T_{bm}^+ & \tilde{\mathcal{H}}_m & T_{tm} \\ 0 & T_{tm}^+ & \mathcal{H}_N \end{pmatrix}, \quad (1)$$

where  $\mathcal{H}_1$  and  $\mathcal{H}_N$  describe the bottom (1st) and top ( $N$ th) TMD layer, respectively.  $\tilde{\mathcal{H}}_m$  represents the middle  $N - 2$  layers.

For the outermost two layers,

$$\mathcal{H}_{1/N} = -\frac{\hbar^2 (\mathbf{k} - \kappa_{1/N})^2}{2m^*} + \Delta(\mathbf{r}, \theta_{1/N}), \quad (2)$$

where  $\theta_{1/N}$  is the twist angle of the 1st/ $N$ th monolayer, and  $\kappa_{1/N}$  is the corresponding momentum offset. As shown in Fig. 1, for the alternating twist case, we always assume the twist angle of the odd (even) layer is  $\theta/2$  ( $-\theta/2$ ), and the momentum offset is  $\kappa_+$  ( $\kappa_-$ ) for the odd (even) layer, where  $\kappa_{\pm} = [4\pi/(3a_M)](-\sqrt{3}/2, \mp 1/2)$ .  $a_M = a_0/\theta$  is the period of the moiré potential, and  $a_0$  is the lattice constant of the TMD monolayer.  $\Delta(\mathbf{r}, \theta)$  describes the layer-dependent moiré potential

$$\Delta(\mathbf{r}, \theta) = 2V \sum_{j=1,3,5} \cos(\mathbf{g}_j \cdot \mathbf{r} + \eta\psi), \quad (3)$$

where  $\mathbf{g}_j$  is  $(j - 1)\pi/3$  counterclockwise rotation of the moiré reciprocal lattice vector  $\mathbf{g}_1 = (4\pi/\sqrt{3}a_M, 0)$ .  $\eta(\theta) = \text{sign}(\theta)$  denotes the direction of the rotation, e.g.  $\eta(\theta/2) = 1$ . For MoTe<sub>2</sub>, we set  $a_0 = 3.472\text{\AA}$ ,  $V = 8$  meV,  $\psi = -89.6^\circ$ , and the effective mass  $m^* = 0.62 m_e$ <sup>6,54</sup>.

For the middle  $N - 2$  layers, the Hamiltonian  $\tilde{\mathcal{H}}_m$  is,

$$\tilde{\mathcal{H}}_m = \begin{pmatrix} \mathcal{H}_2 & \Delta_T^\dagger(\mathbf{r}) & 0 & \cdots & 0 \\ \Delta_T(\mathbf{r}) & \mathcal{H}_3 & \Delta_T(\mathbf{r}) & \cdots & 0 \\ 0 & \Delta_T^\dagger(\mathbf{r}) & \mathcal{H}_4 & \cdots & 0 \\ \vdots & \vdots & \vdots & \ddots & \vdots \\ 0 & 0 & 0 & \cdots & \mathcal{H}_{N-1} \end{pmatrix} \quad (4)$$

where  $\mathcal{H}_i$  is the Hamiltonian of the  $i$ -th layer with  $1 < i < N$ .

$$\mathcal{H}_i = -\frac{\hbar^2 (\mathbf{k} - \kappa_i)^2}{2m^*} + 2\Delta(\mathbf{r}, \theta_i) \quad (5)$$

where  $i = 2, 3, \dots, N - 1$  is the layer index.  $\kappa_i$  and  $\theta_i$  are the momentum offset and twist angle of the  $i$ th layer as defined before. Note that the  $i$ th layer here feels the moiré potential from both the  $(i - 1)$ th and  $(i + 1)$ th layers, which thus is distinct from the top and bottom layers in Eq. (2).  $\Delta_T$  is the interlayer tunneling

$$\Delta_T(\mathbf{r}) = w(1 + e^{-i\mathbf{g}_2 \cdot \mathbf{r}} + e^{-i\mathbf{g}_3 \cdot \mathbf{r}}). \quad (6)$$

where  $w = -8.5$  meV is the interlayer tunneling strength<sup>6</sup>.

The interlayer tunneling terms in Eq. (1) are

$$\begin{aligned} T_{bm} &= (\Delta_T(\mathbf{r}), 0, \dots, 0) \\ T_{tm} &= (0, \dots, 0, \Delta_T(\mathbf{r})) \end{aligned} \quad (7)$$

### B. Decomposition rules

Firstly, for an  $N$ -layer ATML-MoTe<sub>2</sub>, it should be noted that its electronic states near  $E_f$ , i.e., the moiré flat bands, mainly originate from the middle  $N - 2$  layers  $\tilde{\mathcal{H}}_m$ , with little influence from the outermost two layers. It is because, as shown in Eq. (2) and (5), the moiré potential on the outermost two layers is  $\Delta$ , while

that of the middle layers is  $2\Delta$ . The difference of moiré potential is significant, causing the electronic states of the outermost two layers to be far from the  $E_f$ . Therefore, it is a good approximation to use the electronic structure of  $\tilde{H}_m$  to understand the moiré band structures of ATML-MoTe<sub>2</sub> near  $E_f$ , where the influence of the outermost two layers can be disregarded. The numerical results show that such an approximation works quite well when  $\theta$  is small. Hereafter, we always use  $N$  to refer to the total number of layers in an ATML-MoTe<sub>2</sub>.

Very interestingly,  $\tilde{H}_m$  here has an even-odd dependent decomposition rule, due to its alternating twist configuration. The decomposition rule here is very similar to that of the ATFLG. First, the middle  $N - 2$  layers in  $\tilde{H}_m$  can be divided into two sets, i.e.  $\{H_i|i \in \text{even}\}$  and  $\{H_i|i \in \text{odd}\}$ , where  $H_i$  are identical in each set due to the alternating twist structure. As is proved in Ref. 55, such kind of Hamiltonian matrix can be decomposed using singular value decomposition scheme. This decomposition depends on whether the layer number of  $\tilde{H}_m$ , i.e.  $(N - 2)$ , is even or odd:

$$\tilde{\mathcal{H}}_m^{dec} = \begin{cases} \oplus_{\nu=1}^n h(\lambda_\nu), & \text{if } N-2 \text{ is even,} \\ \oplus_{\nu=1}^n h(\lambda_\nu) \oplus \mathcal{H}_2, & \text{if } N-2 \text{ is odd,} \end{cases} \quad (8)$$

where  $\lambda_\nu = 2 \cos \frac{\pi\nu}{N-1}$  with  $\nu = 1, \dots, n$  and  $n = [(N - 2)/2]$ . Here,  $h(\lambda_\nu)$  is an effective twisted TMD homobilayer with coupling parameter  $\lambda_\nu$

$$h(\lambda_\nu) = \begin{pmatrix} \mathcal{H}_2 & \lambda_\nu \Delta_T(\mathbf{r})^\dagger \\ \lambda_\nu \Delta_T(\mathbf{r}) & \mathcal{H}_3 \end{pmatrix}. \quad (9)$$

where  $H_2$  actually represents a twisted heterobilayers, i.e. an effective TMD monolayer under a moiré potential as given in Eq. (5). Note that, in Eq. (8) and (9),  $H_2$  ( $H_3$ ) is used to denote an effective TMD monolayer with a twist angle  $-\theta/2$  ( $\theta/2$ ). The decomposition above implies that, near  $E_f$ , the moiré bands of  $N$ -layer ATML-MoTe<sub>2</sub> can be approximately decoupled into those of several twisted TMD homobilayers (and a TMD monolayer with a moiré potential) if  $N$  is even (odd).

Furthermore, each  $h(\lambda_\nu)$ , as a twisted TMD homobilayers, will provide two moiré flat bands near  $E_f$ , and the  $H_2$  in Eq. (8) will offer one isolated moiré flat band at  $E_f$ , similar as the twisted TMD heterobilayers. So, the decomposition rules in Eq. (8) actually imply that, with a small  $\theta$ , an  $N$ -layer ATML-MoTe<sub>2</sub> should always exhibit  $N - 2$  moiré flat bands near  $E_f$ .

In addition to the decomposition rule with Eq. (8), an  $N$ -layer ATML-MoTe<sub>2</sub> with odd  $N$  exhibits mirror symmetry relative to the middle monolayer, resulting in a mirror symmetry decomposition as well<sup>30,56</sup>. It should be noted that the mirror symmetry decomposition here is exact, but the decomposition in Eq. (8) is only valid for the moiré bands very near  $E_f$ .

### III. RESULTS AND DISCUSSION

In this section, we show our numerical results about the ATML-MoTe<sub>2</sub>, where the cases of even and odd  $N$  are discussed separately.

#### A. Odd-layer ATML-MoTe<sub>2</sub>

##### 1. AT3L-MoTe<sub>2</sub>

We first consider the case of AT3L-MoTe<sub>2</sub> ( $N = 3$ ). As we will see, an AT3L-MoTe<sub>2</sub> always has one moiré flat band near  $E_f$ , which is approximately equivalent to a triangle lattice Hubbard model resembling the twisted TMD heterobilayers when  $\theta$  is small.

The AT3L-MoTe<sub>2</sub> has a mirror symmetry relative to the middle monolayer. So, as mentioned in the last section, we can do a mirror symmetry decomposition for its moiré bands. To do the mirror symmetry decomposition, we first have to build a parity-resolved basis  $\{|\phi_{1,3}, e\rangle, |\phi_2, e\rangle, |\phi_{1,3}, o\rangle\}$  according to the mirror symmetry, where

$$\begin{aligned} |\phi_{1,3}, e\rangle &= \frac{1}{\sqrt{2}}(|\phi_1\rangle + |\phi_3\rangle), \\ |\phi_2, e\rangle &= |\phi_2\rangle, \\ |\phi_{1,3}, o\rangle &= \frac{1}{\sqrt{2}}(|\phi_1\rangle - |\phi_3\rangle). \end{aligned} \quad (10)$$

Here,  $e/o$  denotes the even/odd parity relative to the middle monolayer.  $|\phi_{1,2,3}\rangle$  are the original basis functions of the 1st, 2nd, 3rd monolayers, used in the Hamiltonian (1). This parity-resolved basis gives rise to a transformation matrix,

$$U = \frac{1}{\sqrt{2}} \begin{pmatrix} 1 & 0 & 1 \\ 0 & \sqrt{2} & 0 \\ 1 & 0 & -1 \end{pmatrix}. \quad (11)$$

Under this transformation, we get a decoupled Hamiltonian  $\mathcal{H}'_{mirr} = U^{-1}\mathcal{H}U$ , where

$$\mathcal{H}'_{mirr} = \begin{pmatrix} \mathcal{H}_1 & \sqrt{2}\Delta_T(\mathbf{r}) & 0 \\ \sqrt{2}\Delta_T^\dagger(\mathbf{r}) & \mathcal{H}_2 & 0 \\ 0 & 0 & \mathcal{H}_3 \end{pmatrix}. \quad (12)$$

We see that the Hamiltonian of AT3L-MoTe<sub>2</sub> is now decoupled into two subsystems with opposite parity. Formally, the part with even parity is very like twisted TMD homobilayers with the interlayer tunneling scaled by  $\sqrt{2}$ , while the part with odd parity is equivalent to a TMD monolayer with an applied moiré potential, i.e.  $H_3$ . An important fact is that the moiré potentials in  $H_{1,3}$  are largely different from that in  $H_2$ , so that the electron states from  $H_{1,3}$  are pushed far away from the  $E_f$ , especially when  $\theta$  is small. Therefore, at a small twist angle, the moiré bands of AT3L-MoTe<sub>2</sub> near  $E_f$  mainly originate the middle monolayer  $H_2$  with even parity. If we

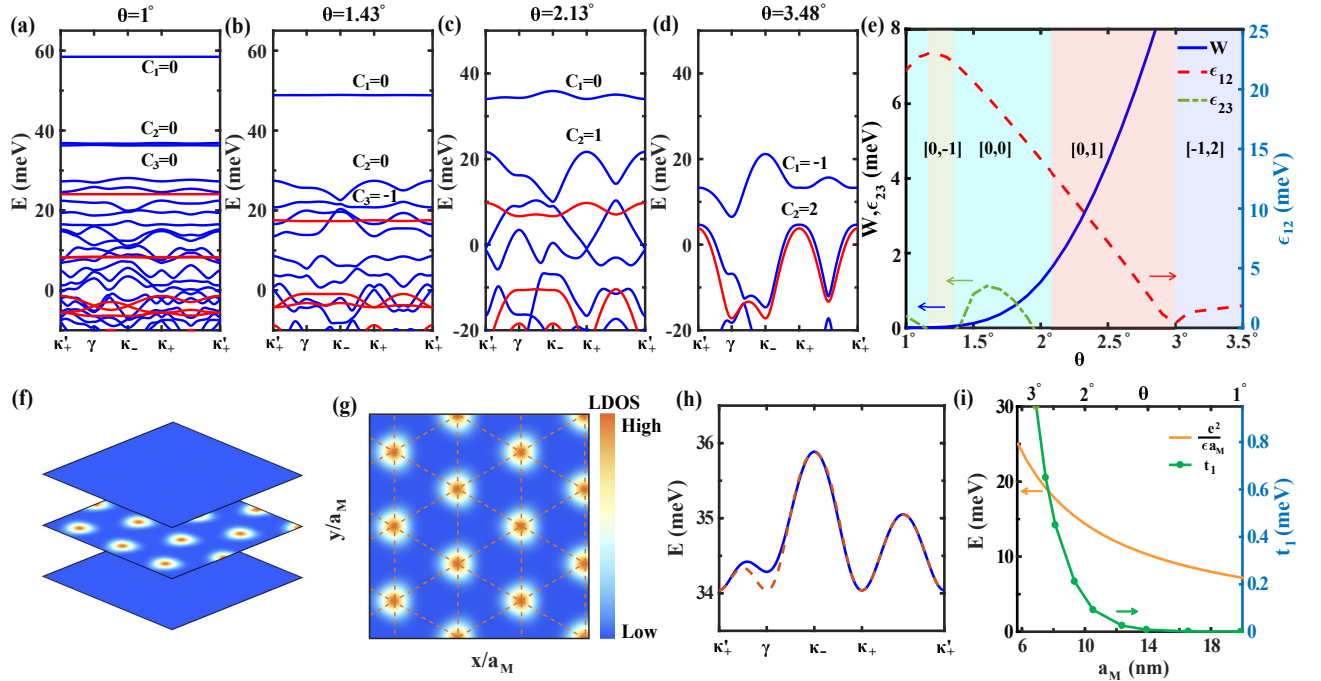


FIG. 2. (a)-(d) The moiré band structures of AT3L-MoTe<sub>2</sub> for (a)  $\theta = 1^\circ$ , (b)  $1.43^\circ$ , (c)  $2.13^\circ$ , and (d)  $3^\circ$ . Blue (red) lines represent the bands with even (odd) parity. (e) The bandwidth  $W$  for the 1st band, and the energy gap  $\epsilon_{12}$  ( $\epsilon_{23}$ ) between the 1st (2nd) and 2nd (3rd) bands as a function of  $\theta$ . By using different colors to identify the various regions of  $\theta$ , the top two moiré bands have distinct Chern numbers  $[C_1, C_2]$  within these regions. (f) shows the 1st flat band wave function distribution in each layer of the AT3L-MoTe<sub>2</sub>, which correspond to the  $\gamma$  point for  $\theta = 2.13^\circ$ . (g) We present the wave function distribution of the middle layer. (h) The blue solid line is the 1st band of AT3L-MoTe<sub>2</sub> at  $\theta = 2.13^\circ$ , which is the enlarged view of the 1st band in (c). The orange dashed line is a tight-binding-model fit to this band that includes hopping up to the 3rd nearest-neighbor. (i) The yellow solid line is a characteristic interaction energy scale for  $\epsilon = 10$ , and the green solid line is the nearest-neighbor hopping parameter  $t_1$  as a function of moiré period  $a_M$ .

further note that  $H_2$  here is nearly identical to the Hamiltonian of a twisted TMD heterobilayers (e.g. WSe<sub>2</sub>/WS<sub>2</sub>) in form, which hosts one isolated moiré flat band at  $E_f$ , described by a triangle lattice Hubbard model<sup>41–43</sup>. It can be expected that, when  $\theta$  is small, an AT3L-MoTe<sub>2</sub> will have a single isolated moiré flat band (even parity) near  $E_f$ , similar to the one in WSe<sub>2</sub>/WS<sub>2</sub> system, which can be described by a triangle lattice Hubbard model.

However, we emphasize that this picture of the triangle lattice Hubbard model is only valid for small twist angle regions. It is because, as  $\theta$  approaches  $3^\circ$ , the moiré band from  $H_{1,3}$  in Eq. (12) will approach that of  $H_2$ , and the hybridization between them cannot be ignored. In other words, when  $\theta$  becomes large enough, the part with even parity in Eq. (12) will behave more like a twisted TMD homobilayers, instead of a twisted TMD heterobilayers, and the 1st moiré band near  $E_f$  will get a nonzero Chern number then.

The numerical results of the moiré bands for AT3L-MoTe<sub>2</sub> with various twist angles are given in Fig. 2, where blue (red) lines represent the bands with even (odd) parity. Fig. 2 (a) shows the moiré band structure at  $\theta = 1^\circ$ . As we expected, at such small  $\theta$ , we do get an isolated moiré flat band near  $E_f$ , which is separated from other moiré bands by a large gap of about 20 meV. Meanwhile,

the odd parity bands (red lines) are far away from the  $E_f$ , so that the three topmost moiré bands are all with even parity (blue lines). According to the analysis above, we in fact can consider that the three topmost moiré bands mainly originate from an equivalent twisted TMD heterobilayers like WSe<sub>2</sub>/WS<sub>2</sub>, where the first one is a moiré  $s$ -band. The numerical results indicate that these three moiré bands are topologically trivial, i.e. Chern number is zero, when  $\theta$  is small.

The bandwidth of the 1st moiré band  $W$  increases monotonically as  $\theta$  increases, see Fig. 2 (e). We see that when  $\theta < 1.5^\circ$ , the 1st moiré band is almost completely flat as shown in Fig. 2 (b). In Fig. 2 (e), we also plot the gap between the 1st moiré band and other low energy bands, i.e.  $\epsilon_{12}$ , as a function of  $\theta$ . And the gap between the 2nd and 3rd moiré bands  $\epsilon_{23}$  is also shown in Fig. 2 (e) as well. As  $\theta$  becomes larger,  $\epsilon_{12}$  nearly monotonically decreases, and it becomes zero when  $\theta$  approaches  $3^\circ$ . Thus, in the regime of  $\theta < 3^\circ$ , the 1st moiré band remains isolated and its Chern number stays at zero, see Fig. 2 (c).

Due to the similarity with the WSe<sub>2</sub>/WS<sub>2</sub> system, we expect that the 1st moiré band here should be approximately equivalent to a triangle lattice Hubbard model when  $\theta$  is small. To verify this prediction, we first calcu-

late the wave function of the 1st moiré flat band ( $\gamma$  point,  $\theta = 2.13^\circ$ ), as shown in Fig. 2 (f) and (g). The numerical results show that the wave function distribution of the 1st moiré band is mainly localized in the middle monolayer, and the wave function distribution of clearly forms a triangle lattice, as we expect. In this situation, the influence of the outermost two layers, i.e.  $H_{1,3}$  in Eq.(12), is small, so that the triangle lattice Hubbard model is a rather good approximation. This is also demonstrated clearly by the fitting of the 1st moiré band with a tight binding model of triangle lattice, as given in Fig. 2 (h). The characteristic Coulomb energy  $\frac{e^2}{\epsilon a_M}$ , which is proportional to the on-site Hubbard  $U_0$ , is plotted in Fig. 2 (i). And, the nearest-neighbor (NN) hopping parameter  $t_1$  of the triangle lattice model got by fitting the 1st moiré band as a function of moiré period  $a_M$  is given in Fig. 2 (i) as well. Note that the exotic correlated states in twisted TMD heterobilayers have been intensively studied recently<sup>41–43,57–70</sup>.

With a larger  $\theta$ , the 2nd and 3rd moiré bands can have a nonzero Chern number once touching with other moiré bands occurs. Note that the Chern number hereafter is for one valley, and the other valley has the opposite Chern number due to the time reversal symmetry. In Fig. 2 (b), the Chern number of the 3rd moiré band becomes  $C_3 = -1$  when  $\theta = 1.43^\circ$ . And with  $\theta = 2.13^\circ$ , the 2nd moiré band has a nonzero Chern number  $C_2 = 1$ , see Fig. 2 (c). Interestingly, as  $\theta$  increases and crosses  $3^\circ$ , the gap  $\epsilon_{12}$  will first close and reopen, so that the 1st moiré band gets a nonzero Chern number  $C_1 = -1$  once  $\theta > 3^\circ$ , see Fig. 2 (d). As analyzed above, in this case, the triangle lattice Hubbard model becomes invalid for the 1st moiré band. Based on our numerical calculations above, we then can identify various regions of  $\theta$  in Fig. 2 (e), denoted by different colors, in which the moiré bands have distinct Chern numbers [ $C_1, C_2$ ] (the 3rd moiré band is hard to be accessed in the experiment).

Finally, we would like to mention that the moiré band structures of AT3L-MoTe<sub>2</sub> have been also discussed in two other recent papers, but the numerical results are analyzed from a completely different perspective<sup>71,72</sup>. The decomposition of moiré bands, the analysis of the origination of the 1st moiré band, and the prediction about the equivalent Hubbard model are the focus of this work. Meanwhile, we also notice the twisted TMD homotrilayer systems have been successfully fabricated in recent experiments<sup>73–77</sup>.

## 2. AT5L-MoTe<sub>2</sub>

The case of AT5L-MoTe<sub>2</sub> ( $N = 5$ ) is more complex. According to the decomposition rule in Eq. (8), we can expect that, when  $\theta$  is not too large, AT5L-MoTe<sub>2</sub> should have three moiré flat bands near  $E_f$  isolated from other low energy bands, which are mainly from the middle three monolayers.

Note that all the ATML-MoTe<sub>2</sub> with odd  $N$

have mirror symmetry relative to the middle monolayer. So, we can also do the mirror symmetry decomposition for the AT5L-MoTe<sub>2</sub>. Similarly, we first needed to build a parity-resolved basis  $\{|\phi_{1,5}, e\rangle, |\phi_{2,4}, e\rangle, |\phi_3, e\rangle, |\phi_{2,4}, o\rangle, |\phi_{1,5}, o\rangle\}$ , where

$$\begin{aligned} |\phi_{1,5}, e\rangle &= \frac{1}{\sqrt{2}}(|\phi_1\rangle + |\phi_5\rangle) \\ |\phi_3, e\rangle &= |\phi_3\rangle \\ |\phi_{1,5}, o\rangle &= \frac{1}{\sqrt{2}}(|\phi_1\rangle - |\phi_5\rangle) \end{aligned} \quad (13)$$

Based on this basis, we get the following transformation matrix,

$$U = \frac{1}{\sqrt{2}} \begin{pmatrix} 1 & 0 & 0 & 0 & 1 \\ 0 & 1 & 0 & 1 & 0 \\ 0 & 0 & \sqrt{2} & 0 & 0 \\ 0 & 1 & 0 & -1 & 0 \\ 1 & 0 & 0 & 0 & -1 \end{pmatrix}. \quad (14)$$

After the transformation, a decoupled Hamiltonian is achieved

$$\mathcal{H}'_{mirr} = \begin{pmatrix} \mathcal{H}_1 & \Delta_T(\mathbf{r}) & 0 & 0 & 0 \\ \Delta_T^\dagger(\mathbf{r}) & \mathcal{H}_2 & \sqrt{2}\Delta_T^\dagger(\mathbf{r}) & 0 & 0 \\ 0 & \sqrt{2}\Delta_T(\mathbf{r}) & \mathcal{H}_3 & 0 & 0 \\ 0 & 0 & 0 & \mathcal{H}_4 & \Delta_T^\dagger(\mathbf{r}) \\ 0 & 0 & 0 & \Delta_T(\mathbf{r}) & \mathcal{H}_5 \end{pmatrix}. \quad (15)$$

In this decoupled Hamiltonian, the part with even parity is equivalent to an alternating twisted TMD trilayer with asymmetric interlayer tunneling, where the one between  $H_2$  and  $H_3$  is scaled by  $\sqrt{2}$ . Meanwhile, the odd parity part is an equivalent twisted TMD bilayer.

Similar to that in AT3L-MoTe<sub>2</sub>, the moiré potentials in the outermost two layers ( $H_{1,5}$ ) are significantly different from those in the middle three monolayers, which makes the electronic states from  $H_1$  and  $H_5$  far from the  $E_f$ , especially at small twist angle. So, in the small twist angle region, the even parity part will behave like the twisted TMD homobilayers, which offers a pair of moiré flat bands near  $E_f$ . Similarly, the odd parity part will host one isolated moiré flat band at  $E_f$ , which originates from the  $H_4$ . Therefore, the mirror symmetry decomposition here indicates that AT5L-MoTe<sub>2</sub> exhibits three moiré flat bands at  $E_f$  for a small twist angle, which is in good agreement with the deduction of the decomposition rule in Eq. (8). Actually, Eq. (8) also indicates that AT5L-MoTe<sub>2</sub> can be decoupled into one twisted TMD homobilayers  $h(\lambda_{\nu=1})$  and one twisted heterobilayers described as  $H_4$ .

The numerical results of the moiré bands of AT5L-MoTe<sub>2</sub> are given in Fig. 3. In Fig. 3 (a-d), we plot the moiré bands of AT5L-MoTe<sub>2</sub> for different twist angles, where the blue (red) lines are for the even (odd) parity. As expected, when  $\theta$  is small, AT5L-MoTe<sub>2</sub> does have

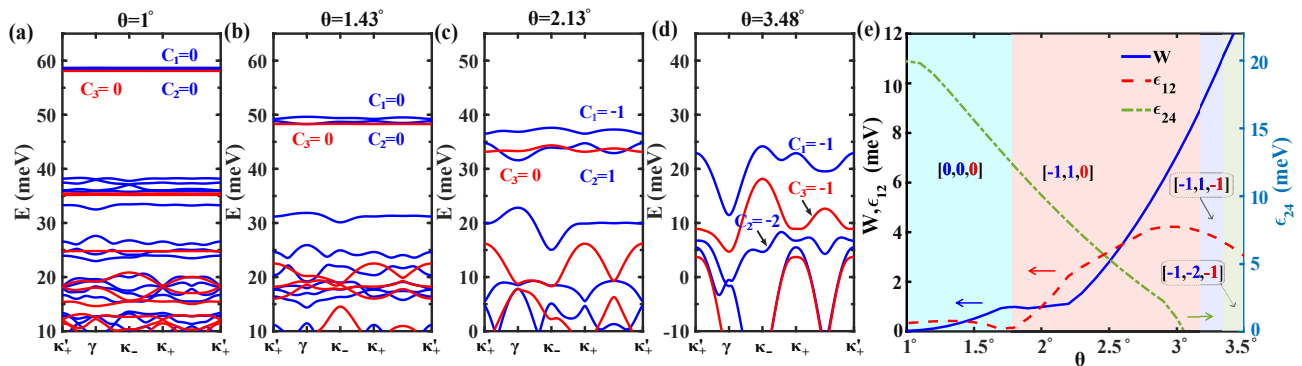


FIG. 3. The moiré band structures of AT5L-MoTe<sub>2</sub> for (a)  $\theta = 1^\circ$ , (b)  $1.43^\circ$ , (c)  $2.13^\circ$ , and (d)  $3.48^\circ$ . Blue (red) lines represent the bands with even (odd) parity. In (e), we plot  $W$ ,  $\epsilon_{12}$  and  $\epsilon_{24}$  as functions of  $\theta$ .  $W$  is the bandwidth of the 1st band.  $\epsilon_{12}$  ( $\epsilon_{24}$ ) is the gap between the 1st (2nd) and 2nd (4th) bands. Here, the 1st, 2nd and 4th bands refer to the three topmost even parity bands (blue lines), while the 3rd band is the topmost odd parity band (red lines). The regions with different Chern numbers  $[C_1, C_2, C_3]$  are denoted by different colors.

three moiré flat bands at  $E_f$ , isolated from other low energy bands by an obvious gap, see Fig. 3 (a-c). Here, two of the three moiré flat bands with even parity (blue lines) behave like that of a twisted MoTe<sub>2</sub> homobilayers, while the left one (red lines, odd parity) corresponds to the moiré flat band of a twisted TMD heterobilayers.

At a small twist angle  $\theta = 1^\circ$ , the three moiré flat bands are nearly degenerate at  $E_f$ , see Fig. 3 (a). Such threefold degeneracy of the moiré flat bands here will give rise to a giant DOS at  $E_f$ , which may induce exotic correlated insulating states in experiments. Increasing  $\theta$ , the bandwidth of the moiré flat bands increases and a gap between the two even parity flat bands (blue lines) becomes observable, as shown in Fig. 3 (b) and (c). In the region  $3.2^\circ > \theta > 1.8^\circ$  [Fig. 3 (b) and (c)], the Chern number of the two even parity flat bands becomes nonzero, i.e.  $[C_1, C_2] = [-1, 1]$  like that in twisted MoTe<sub>2</sub> homobilayers, while that of the odd parity flat band (red lines) remains zero, i.e.  $C_3 = 0$ . When  $\theta$  is large enough, e.g.  $\theta = 3.48^\circ$  in Fig. 3 (d), the three moiré flat bands are no longer isolated from other low energy bands, and the Chern numbers are changed accordingly, i.e.  $[C_1, C_2, C_3] = [-1, -2, -1]$ .

In Fig. 3 (e), we plot the  $W$ ,  $\epsilon_{12}$  and  $\epsilon_{24}$  as functions of  $\theta$ . Here,  $W$  is the bandwidth of the 1st moiré flat band,  $\epsilon_{12}$  is the gap between the two even parity moiré flat bands, and  $\epsilon_{24}$  represents the gap between the 2nd moiré flat band and the 4th moiré band (blue, even parity). We also denote the regions of  $\theta$  with different Chern numbers by different colors, as shown in Fig. 3 (e). We see that, though  $W$  increases monotonically with  $\theta$ , the AT5L-MoTe<sub>2</sub> does not have a clear magic angle. In principle, in the region  $1.8^\circ < \theta < 2.2^\circ$ , we can get an isolated moiré flat band at  $E_f$ , separated from other moiré bands with a small but detectable gap.

## B. Even-layer ATML-MoTe<sub>2</sub>

In this section, we then discuss the moiré band structures of the ATML-MoTe<sub>2</sub> with even  $N$ .

### 1. AT4L-MoTe<sub>2</sub>

We first consider the case of AT4L-MoTe<sub>2</sub>. The numerical results are shown in Fig. 4, where the moiré band structures of AT4L-MoTe<sub>2</sub> at different twist angles are given, as illustrated in Fig. 4 (a)-(f).

For AT4L-MoTe<sub>2</sub>, the most prominent feature is that, at a small twist angle, it always exhibits two moiré flat bands at  $E_f$ , which are separated from the remaining moiré bands by a large gap. This is quite like the twisted MoTe<sub>2</sub> homobilayers, as indicated by the decomposition rules in Eq. (8). Note that the ATML-MoTe<sub>2</sub> with even  $N$  does not have mirror symmetry anymore. The two moiré flat bands exhibit distinct behaviors across different regions of  $\theta$ , and three regions of  $\theta$  are identified according to their distinct topological features:

When  $\theta \lesssim 1.4^\circ$ , the two moiré flat bands are nearly degenerate at the  $E_f$ , which are separated from other bands by a large gap. The Chern numbers of the first two flat bands are  $[C_1, C_2] = [0, 0]$  in this region, as indicated in Fig. 4 (a) and (g). The case of  $\theta = 1^\circ$  is plotted in Fig. 4 (a). As shown in Fig. 4(g), the minimum value of the bandwidth  $W$  of the first flat band occurs around  $\theta = 1^\circ$ . Meanwhile,  $\epsilon_{23}$  has its maximum value about 21.48 meV around  $\theta \approx 1.1^\circ$ .

Increasing  $\theta$  to the region  $1.4^\circ < \theta < 3.3^\circ$ , the degeneracy of the two moiré flat bands is lifted, and the gap  $\epsilon_{12}$  becomes obvious. Meanwhile, the Chern numbers of the two moiré bands become nonzero, i.e.  $[-1, 1]$ . We thus can get an isolated topological flat band near  $E_f$ . In this region, we plot  $\theta = 1.43^\circ$  in Fig. 4(b), where a sudden change of the Chern number occurs near  $\theta \approx 1.4^\circ$ . The gap between the two moiré flat bands is observable when

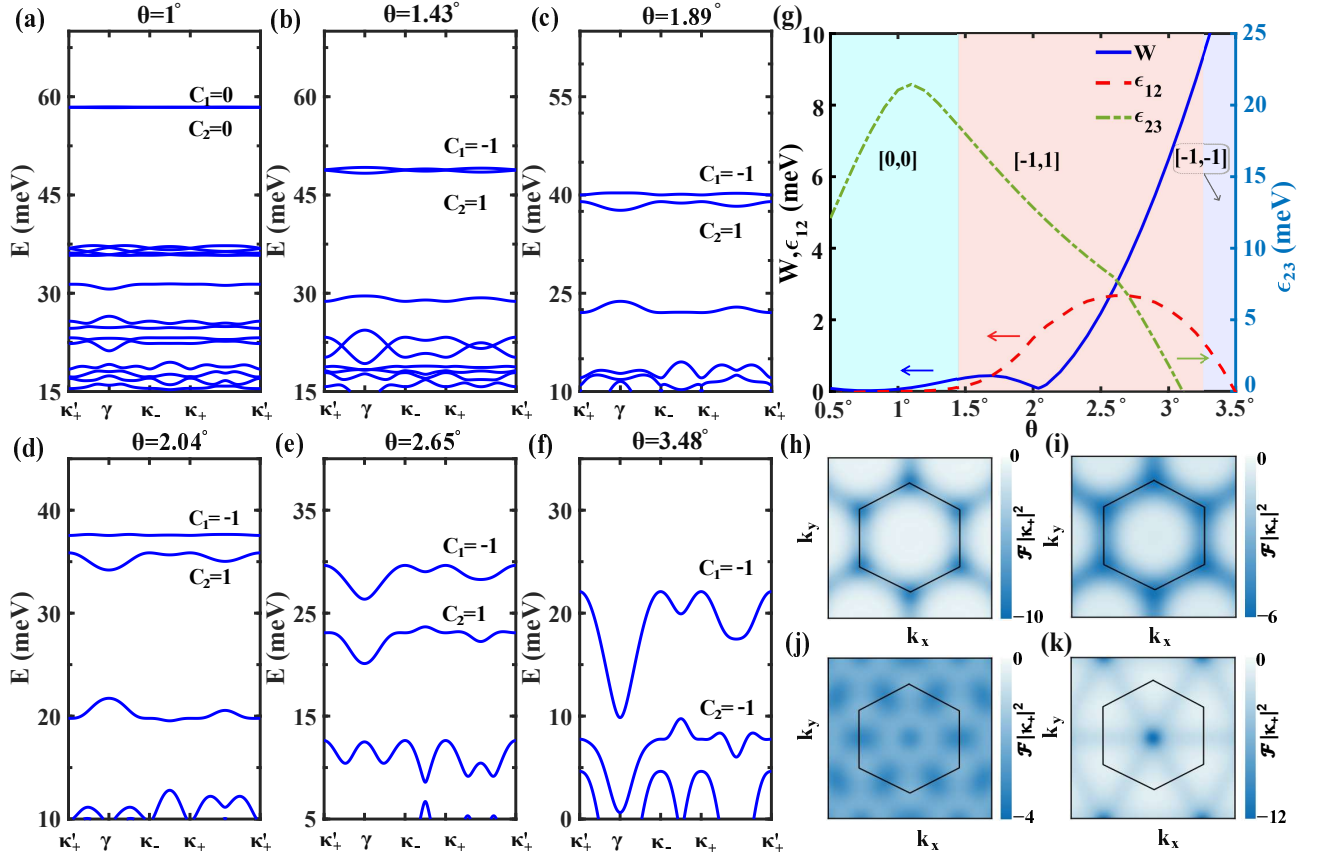


FIG. 4. (a)-(f) The moiré band structures of AT4L-MoTe<sub>2</sub> for twist angle  $\theta = 1^\circ, 1.43^\circ, 1.89^\circ, 2.04^\circ, 2.65^\circ, 3^\circ$ . (g) The bandwidth  $W$  of the 1st band (solid blue line), the gap  $\epsilon_{12}$  between the 1st and 2nd bands (dashed red line), and the gap  $\epsilon_{23}$  between the 2nd and 3rd bands (dashed green line) as a function of twist angle. Different colored regions represent different Chern numbers of the top two bands. (h)-(k) show the distribution of Berry curvature  $\mathcal{F}$  for (h)  $\theta = 1.89^\circ$ , (i)  $\theta = 2.04^\circ$ , (j)  $\theta = 2.65^\circ$ , and (k)  $\theta = 3.48^\circ$ .

$\theta = 1.89^\circ$ , see Fig. 4(c). Most interestingly, we find a magic angle around  $\theta \approx 2.02^\circ$ , where the bandwidth of the 1st moiré flat band becomes as small as 0.1 meV, as shown in Fig. 4(d) and (g). Further increasing  $\theta$  to  $2.65^\circ$ , the two moiré bands become more dispersive, see Fig. 4(e). When  $\theta$  approaches about  $3.1^\circ$ , the gap  $\epsilon_{23}$  becomes zero, see Fig. 4 (g).

In the region of  $\theta > 3.3^\circ$ , we find a change of Chern number from  $[-1, 1]$  to  $[-1, -1]$ , see Fig. 4(f) and (g). In this region, the bandwidth of the first two moiré bands will increase monotonically as  $\theta$  increases. Consequently, the two bands gradually begin to overlap in energy, i.e.  $\epsilon_{12} = 0$ , though they are still isolated from each other.

As well known, in order to realize FQAH state, the presence of a topological flat band is essential<sup>78–86</sup>. And recent works indicates that the uniformity of Berry curvature may also play an important role<sup>17</sup>. Thus, we then discuss Berry curvature  $\mathcal{F}(\mathbf{k})$  of the top flat band at different  $\theta$ . The  $\mathcal{F}(\mathbf{k})$  in Fig. 4(h)-(k) corresponds to the band structures depicted in Fig. 4(c)-(f), respectively. With a small twist angle, e.g.  $\theta = 1.89^\circ$  in Fig. 4(h),  $\mathcal{F}$  is sharply peaked at the  $\kappa_{\pm}$  points. As  $\theta$  increases,  $\mathcal{F}$

will first spread along the "bond" directions between the adjacent  $\kappa_{\pm}$  points, as shown in Fig. 4(i) with  $\theta = 2.04^\circ$ . Increasing  $\theta$  further,  $\mathcal{F}$  will shift from  $\kappa_{\pm}$  to  $\gamma$ . Around  $\theta = 2.65^\circ$ ,  $\mathcal{F}$  becomes almost uniform in the whole moiré Brillouin zone, see Fig. 4(j). This uniform distribution of  $\mathcal{F}$  reminds us of Landau levels, which is also similar to the twisted MoTe<sub>2</sub> homobilayers<sup>17</sup>. In Fig. 4(k), we plot  $\mathcal{F}$  at  $\theta = 3.48^\circ$ , where  $\mathcal{F}$  is peaked around  $\gamma$  point.

Based on the results above, we see that AT4L-MoTe<sub>2</sub> shares similarities with the twisted MoTe<sub>2</sub> homobilayers, while also exhibiting difference. The similarities are they both have a pair of topological flat bands, which behave similarly as  $\theta$  increases. The differences are: (1) The AT4L-MoTe<sub>2</sub> has a larger magic angle  $\theta \approx 2.04^\circ$ , while the magic angle of the twisted MoTe<sub>2</sub> homobilayers is about  $1.4^\circ$ ; (2) The Chern number of the two flat bands of the AT4L-MoTe<sub>2</sub> are  $[0, 0]$  when  $\theta < 1.4^\circ$ , but the Chern numbers of the twisted MoTe<sub>2</sub> homobilayers are always nonzero.

Most importantly, our results imply that AT4L-MoTe<sub>2</sub> should also host FQAH state around the magic angle  $\theta \approx 2.04^\circ$  like the twisted MoTe<sub>2</sub> homobilayers, because that their moiré flat bands have nearly the same topological

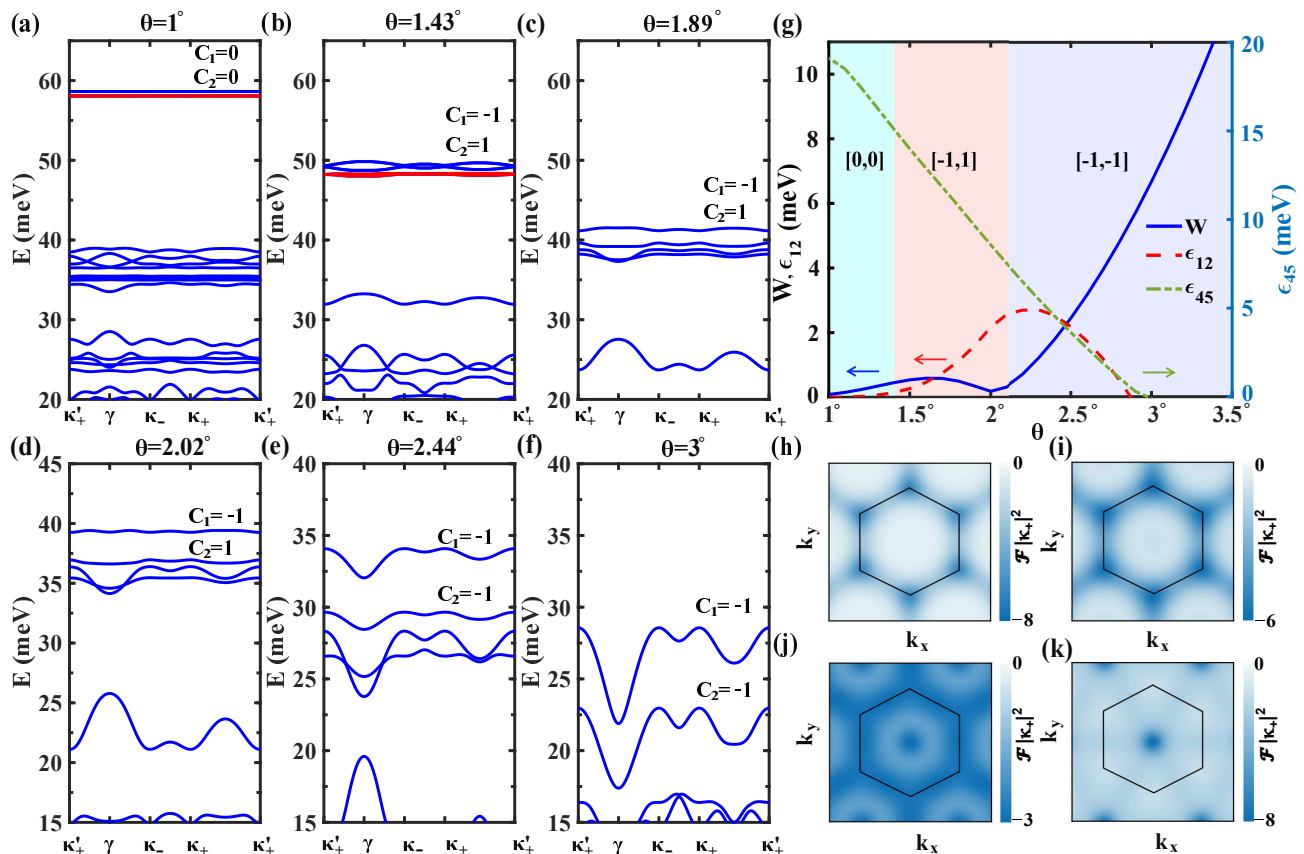


FIG. 5. (a)-(f) The moiré band structures of AT6L-MoTe<sub>2</sub> at different twist angles, corresponding to  $\theta = 1^\circ, 1.43^\circ, 1.89^\circ, 2.02^\circ, 2.44^\circ, 3^\circ$ , respectively. In (a) and (b), the four topmost moiré flat bands can be approximately divided into two equivalent twisted TMD homobilayers (blue and red). (g) The bandwidth  $W$  of the 1st band, the gap  $\epsilon_{12}$  between the 1st and 2nd bands, and the gap  $\epsilon_{45}$  between the 4th and 5th bands as a function of  $\theta$ . (h)-(k) show the distribution of  $\mathcal{F}$  for (h)  $\theta = 1.89^\circ$ , (i)  $2.02^\circ$ , (j)  $2.44^\circ$ , and (k)  $3^\circ$ .

features, e.g. the flat dispersion and uniformity of the Berry curvature near the magic angle. Meanwhile, owing to the similarity between AT4L-MoTe<sub>2</sub> and twisted TMD homobilayers, this system could also serve as an ideal platform for realizing a Hubbard model<sup>6,17,52,87–89</sup>.

## 2. AT6L-MoTe<sub>2</sub>

We then consider the case of AT6L-MoTe<sub>2</sub>, where  $N = 6$ . According to the decomposition rules in Eq. (8), its moiré bands near  $E_f$  can approximately be viewed as originating from two independent twisted TMD homobilayers, i.e.  $h(\lambda_1)$  and  $h(\lambda_2)$ , with different scaling factors  $\lambda_{1,2}$ . Here, each equivalent twisted TMD homobilayers will offer two moiré flat bands at  $E_f$ , thus, in this case, we should obtain four isolated moiré flat bands in the small twist angle region.

The numerical results of AT6L-MoTe<sub>2</sub> are given in Fig. 5. In Fig. 5 (a)-(f), we plot the moiré bands with different  $\theta$ . Clearly, as anticipated, the AT6L-MoTe<sub>2</sub> does exhibit four moiré flat bands near  $E_f$  at a small twist angle, which are separated from other bands by a large

gap and nearly degenerate when  $\theta < 1.4^\circ$ . As analyzed above, when  $\theta$  is small [Fig. 5 (a), (b)], the four moiré flat bands can be further approximately divided into two groups (blue and red), with two bands in each group, where each group here belongs to an equivalent twisted TMD homobilayers, i.e.  $h(\lambda_{1,2})$ . For a large  $\theta$ , this approximation does not work well, since the coupling between the two groups of moiré flat bands will obviously alter the band shape and the Chern number.

Below, we only focus on the two topmost moiré flat bands out of the four. It is because, on one hand, the two topmost moiré flat bands are the most easily accessible bands in experiments, and on the other hand, these two bands can be isolated via adjusting  $\theta$ , allowing their Chern numbers to be well-defined. Thus, as illustrated in Fig. 5 (g), we identify three distinct regions for  $\theta$ , according to the Chern numbers of the two topmost moiré flat bands:

When  $\theta \lesssim 1.4^\circ$ , the Chern numbers of the top two flat bands in this region are  $[C_1, C_2] = [0, 0]$ . In this case, the four moiré flat bands are nearly degenerate near  $E_f$ , as depicted in Fig. 5 (a), which are separated from other bands by a large gap. However, the first two moiré

flat bands are actually isolated, albeit with very small gaps. Therefore, the calculations can yield a well-defined Chern number for the two topmost moiré bands here. In comparison with cases where  $N < 6$ , the four nearly degenerate moiré flat bands in AT6L-MoTe<sub>2</sub> will lead to a significantly larger DOS near  $E_f$ , potentially resulting in exotic correlated insulating states in this region.

When  $1.4 \lesssim \theta \lesssim 2.1^\circ$ , the top two flat bands exhibit non-zero Chern numbers  $[C_1, C_2] = [-1, 1]$  in this range. First, as shown in Fig. 5 (b)-(d), the degeneracy of the moiré flat bands is lifted as  $\theta$  increases. With a larger  $\theta$ , the gap between the two topmost moiré bands, namely  $\epsilon_{12}$ , becomes more apparent in this region, as illustrated in Fig. 5 (g). Consequently, the 1st moiré flat band ( $C_1 = -1$ ) is isolated, as seen in Fig. 5 (c) and (d). Meanwhile, the bandwidth of the 1st moiré band,  $W$ , remains small. In Fig. 5 (g), we plot  $W$  and  $\epsilon_{12}$  as functions of  $\theta$ . This indicates that  $\theta \approx 2.02^\circ$  is a magic angle for the 1st moiré flat band, see Fig. 5 (d), which is quite like the case of AT4L-MoTe<sub>2</sub>. And the gap between the 4nd and 5rd moiré bands  $\epsilon_{45}$  is also shown in Fig. 5 (g) as well. As  $\theta$  becomes larger,  $\epsilon_{45}$  nearly monotonically decreases, and it becomes zero when  $\theta$  approaches  $3^\circ$ .

When  $\theta > 2.1^\circ$ , the Chern numbers of the top two moiré flat bands becomes  $[C_1, C_2] = [-1, -1]$ , as seen in Fig. 5 (g). The cases with  $\theta = 2.44^\circ$  and  $\theta = 3^\circ$  are plotted in Fig. 5 (e) and (f), respectively. In these cases, the top two moiré bands become more dispersive but remain isolated.

The numerical results above imply that the top moiré flat band behaves very like those in twisted MoTe<sub>2</sub> homobilayers and AT4L-MoTe<sub>2</sub>, suggesting it is also an ideal platform for realizing FQAH states. We thus further study the distribution of the Berry curvature  $\mathcal{F}$  of the top moiré flat band at different  $\theta$ , as illustrated in Fig. 5 (h)-(k). At  $\theta = 1.89^\circ$ , the peak of  $\mathcal{F}$  distribution is located at the  $\kappa_\pm$  points, see Fig. 5 (h). When  $\theta$  increases to the magic angle  $2.02^\circ$ , the  $\mathcal{F}$  distribution will gradually shift along the edges of the moiré BZ, as illustrated in Fig. 5 (i). When  $\theta = 2.44^\circ$ , the distribution of  $\mathcal{F}$  becomes uniform, see Fig. 5 (j). At a large  $\theta$ , e.g.  $\theta = 3^\circ$  in Fig. 5 (k),  $\mathcal{F}$  mainly distributes around the  $\gamma$  points. The distribution of  $\mathcal{F}$  here is also very similar to that in twisted MoTe<sub>2</sub> bilayer and AT4L-MoTe<sub>2</sub>, suggesting that the moiré flat bands in these systems will share similar topological features, and thus may host FQAH states.

## IV. SUMMARY

In conclusion, we theoretically investigated the moiré band structures of ATML-MoTe<sub>2</sub>, where the MoTe<sub>2</sub> monolayers are stacked in an alternately twist way.

We first propose an even-odd dependent decomposition rule for the ATML-MoTe<sub>2</sub>, which works quite well when  $\theta$  is small. The decomposition rules first indicate that an  $N$ -layer ATML-MoTe<sub>2</sub> exhibits  $N - 2$  moiré flat bands near  $E_f$ , which relies on the important fact that the outermost two MoTe<sub>2</sub> monolayers actually have little influence on the electronic structures near  $E_f$ , since their moiré potentials are significantly different from the middle ones. This decomposition rule also indicates that when  $N$  is even (odd), ATML-MoTe<sub>2</sub> can be approximately decoupled into several twisted TMD homobilayers (several twisted TMD homobilayers together with one twisted TMD heterobilayers). Meanwhile, we also reveal that the ATML-MoTe<sub>2</sub> also has a mirror symmetry decomposition when  $N$  is odd.

Then, we numerically calculate the moiré band structures of the ATML-MoTe<sub>2</sub> with  $N = 3, 4, 5, 6$ . All the numerical results are in good agreement with the proposed decomposition rules. Most importantly, our numerical calculations give three intriguing predictions:

1. The AT3L-MoTe<sub>2</sub> ( $N = 3$ ) has one isolated moiré flat band, which corresponds to a triangular lattice Hubbard model, resembling the twisted TMD heterobilayers.
2. The AT4L-MoTe<sub>2</sub> ( $N = 4$ ) has two topological flat bands that are very similar to the twisted MoTe<sub>2</sub> homobilayers, implying the possible existence of FQAH states.
3. When  $N > 4$ , the giant DOS induced by the multiple degenerate moiré flat bands may induce exotic correlated states.

Our works reveal that the ATML-MoTe<sub>2</sub> is a promising moiré platform, which not only can be used to simulate the triangle lattice Hubbard model, but also may host the exotic FQAH states, analogous to those observed in twisted MoTe<sub>2</sub> bilayer. We expect that our predictions can be immediately tested in future experiments.

## ACKNOWLEDGMENTS

We appreciate helpful discussions with Professor Fengcheng Wu. This work was supported by the National Natural Science Foundation of China (Grants No. 12141401), the National Key Research and Development Program of China (Grants No. 2022YFA1403501).

---

\* [jinhua@hust.edu.cn](mailto:jinhua@hust.edu.cn)

<sup>1</sup> J. Cai, E. Anderson, C. Wang, X. Zhang, X. Liu, W. Holtz-

- mann, Y. Zhang, F. Fan, T. Taniguchi, K. Watanabe, Y. Ran, T. Cao, L. Fu, D. Xiao, W. Yao, and X. Xu, *Nature* **622**, 63 (2023).
- <sup>2</sup> H. Park, J. Cai, E. Anderson, Y. Zhang, J. Zhu, X. Liu, C. Wang, W. Holtzmann, C. Hu, Z. Liu, T. Taniguchi, K. Watanabe, J.-H. Chu, T. Cao, L. Fu, W. Yao, C.-Z. Chang, D. Cobden, D. Xiao, and X. Xu, *Nature* **622**, 74 (2023).
  - <sup>3</sup> Y. Zeng, Z. Xia, K. Kang, J. Zhu, P. Knüppel, C. Vaswani, K. Watanabe, T. Taniguchi, K. F. Mak, and J. Shan, *Nature* **622**, 69 (2023).
  - <sup>4</sup> K. Kang, B. Shen, Y. Qiu, Y. Zeng, Z. Xia, K. Watanabe, T. Taniguchi, J. Shan, and K. F. Mak, *Nature* **628**, 522 (2024).
  - <sup>5</sup> F. Xu, Z. Sun, T. Jia, C. Liu, C. Xu, C. Li, Y. Gu, K. Watanabe, T. Taniguchi, B. Tong, J. Jia, Z. Shi, S. Jiang, Y. Zhang, X. Liu, and T. Li, *Phys. Rev. X* **13**, 031037 (2023).
  - <sup>6</sup> F. Wu, T. Lovorn, E. Tutuc, I. Martin, and A. H. MacDonald, *Phys. Rev. Lett.* **122**, 086402 (2019).
  - <sup>7</sup> H. Li, U. Kumar, K. Sun, and S.-Z. Lin, *Phys. Rev. Res.* **3**, L032070 (2021).
  - <sup>8</sup> A. P. Reddy, F. Alsallom, Y. Zhang, T. Devakul, and L. Fu, *Phys. Rev. B* **108**, 085117 (2023).
  - <sup>9</sup> C. Wang, X.-W. Zhang, X. Liu, Y. He, X. Xu, Y. Ran, T. Cao, and D. Xiao, *Phys. Rev. Lett.* **132**, 036501 (2024).
  - <sup>10</sup> W.-X. Qiu, B. Li, X.-J. Luo, and F. Wu, *Phys. Rev. X* **13**, 041026 (2023).
  - <sup>11</sup> H. Goldman, A. P. Reddy, N. Paul, and L. Fu, *Phys. Rev. Lett.* **131**, 136501 (2023).
  - <sup>12</sup> C. Xu, J. Li, Y. Xu, Z. Bi, and Y. Zhang, *Proc. Natl. Acad. Sci.* **121**, e2316749121 (2024).
  - <sup>13</sup> A. P. Reddy and L. Fu, *Phys. Rev. B* **108**, 245159 (2023).
  - <sup>14</sup> J. Yu, J. Herzog-Arbeitman, M. Wang, O. Vafek, B. A. Bernevig, and N. Regnault, *Phys. Rev. B* **109**, 045147 (2024).
  - <sup>15</sup> A. Abouelkomsan, A. P. Reddy, L. Fu, and E. J. Bergholtz, *Phys. Rev. B* **109**, L121107 (2024).
  - <sup>16</sup> Y. Zeng, Z. Xia, K. Kang, J. Zhu, P. Knüppel, C. Vaswani, K. Watanabe, T. Taniguchi, K. F. Mak, and J. Shan, *arXiv preprint* (2023), 10.48550/arXiv.2305.00973, arXiv:2305.00973.
  - <sup>17</sup> T. Devakul, V. Crépel, Y. Zhang, and L. Fu, *Nat. Commun.* **12**, 6730 (2021).
  - <sup>18</sup> E. Khalaf, A. J. Kruchkov, G. Tarnopolsky, and A. Vishwanath, *Phys. Rev. B* **100**, 085109 (2019).
  - <sup>19</sup> S. Carr, C. Li, Z. Zhu, E. Kaxiras, S. Sachdev, and A. Kruchkov, *Nano Lett.* **20**, 3030 (2020).
  - <sup>20</sup> C. Lei, L. Linhart, W. Qin, F. Libisch, and A. H. MacDonald, *Phys. Rev. B* **104**, 035139 (2021).
  - <sup>21</sup> J. Shin, B. L. Chittari, and J. Jung, *Phys. Rev. B* **104**, 045413 (2021).
  - <sup>22</sup> Z. Wu, Z. Zhan, and S. Yuan, *Sci. China: Phys., Mech. Astron.* **64**, 267811 (2021).
  - <sup>23</sup> J. M. Park, Y. Cao, K. Watanabe, T. Taniguchi, and P. Jarillo-Herrero, *Nature* **590**, 249 (2021).
  - <sup>24</sup> Z. Hao, A. M. Zimmerman, P. Ledwith, E. Khalaf, D. H. Najafabadi, K. Watanabe, T. Taniguchi, A. Vishwanath, and P. Kim, *Science* **371**, 1133 (2021).
  - <sup>25</sup> Y. Cao, J. M. Park, K. Watanabe, T. Taniguchi, and P. Jarillo-Herrero, *Nature* **595**, 526 (2021).
  - <sup>26</sup> A. Lopez-Bezanilla and J. L. Lado, *Phys. Rev. Res.* **2**, 033357 (2020).
  - <sup>27</sup> B. Xie, R. Peng, S. Zhang, and J. Liu, *npj Comput Mater* **8**, 110 (2022).
  - <sup>28</sup> Z. Ma, S. Li, M. Lu, D.-H. Xu, J.-H. Gao, and X.-C. Xie, *Sci. China Phys. Mech. Astron.* **66**, 227211 (2023).
  - <sup>29</sup> M. Liang, M.-M. Xiao, Z. Ma, and J.-H. Gao, *Phys. Rev. B* **105**, 195422 (2022).
  - <sup>30</sup> S.-P. Ding, M. Liang, Z. Ma, J.-T. Lü, and J.-H. Gao, *Phys. Rev. B* **108**, 195119 (2023).
  - <sup>31</sup> V. Phong, P. A. Pantaleón, T. Cea, and F. Guinea, *Phys. Rev. B* **104**, L121116 (2021).
  - <sup>32</sup> H. D. Scammell, J. Li, and M. S. Scheurer, *2D Mater.* **9**, 025027 (2022).
  - <sup>33</sup> Y. Cao, V. Fatemi, S. Fang, K. Watanabe, T. Taniguchi, E. Kaxiras, and P. Jarillo-Herrero, *Nature* **556**, 43 (2018).
  - <sup>34</sup> Y. Cao, V. Fatemi, A. Demir, S. Fang, S. L. Tomarken, J. Y. Luo, J. D. Sanchez-Yamagishi, K. Watanabe, T. Taniguchi, E. Kaxiras, R. C. Ashoori, and P. Jarillo-Herrero, *Nature* **556**, 80 (2018).
  - <sup>35</sup> R. Bistritzer and A. H. MacDonald, *Proc. Natl. Acad. Sci.* **108**, 12233 (2011).
  - <sup>36</sup> P. Moon and M. Koshino, *Phys. Rev. B* **87**, 205404 (2013).
  - <sup>37</sup> J. Cao, M. Wang, S.-F. Qian, C.-C. Liu, and Y. Yao, *Phys. Rev. B* **104**, L081403 (2021).
  - <sup>38</sup> J. M. Park, Y. Cao, L.-Q. Xia, S. Sun, K. Watanabe, T. Taniguchi, and P. Jarillo-Herrero, *Nat. Mater.* **21**, 877 (2022).
  - <sup>39</sup> Y. Zhang, R. Polski, C. Lewandowski, A. Thomson, Y. Peng, Y. Choi, H. Kim, K. Watanabe, T. Taniguchi, J. Alicea, F. von Oppen, G. Refael, and S. Nadj-Perge, *Science* **377**, 1538 (2022).
  - <sup>40</sup> G. W. Burg, E. Khalaf, Y. Wang, K. Watanabe, T. Taniguchi, and E. Tutuc, *Nat. Mater.* **21**, 884 (2022).
  - <sup>41</sup> F. Wu, T. Lovorn, E. Tutuc, and A. H. MacDonald, *Phys. Rev. Lett.* **121**, 026402 (2018).
  - <sup>42</sup> Y. Tang, L. Li, T. Li, Y. Xu, S. Liu, K. Barmak, K. Watanabe, T. Taniguchi, A. H. MacDonald, J. Shan, and K. F. Mak, *Nature* **579**, 353 (2020).
  - <sup>43</sup> N. Morales-Durán, N. C. Hu, P. Potasz, and A. H. MacDonald, *Phys. Rev. Lett.* **128**, 217202 (2022).
  - <sup>44</sup> S. Fang, R. Kuate Defo, S. N. Shirodkar, S. Lieu, G. A. Tritsarlis, and E. Kaxiras, *Phys. Rev. B* **92**, 205108 (2015).
  - <sup>45</sup> Y. Wang, Z. Wang, W. Yao, G.-B. Liu, and H. Yu, *Phys. Rev. B* **95**, 115429 (2017).
  - <sup>46</sup> M. H. Naik and M. Jain, *Phys. Rev. Lett.* **121**, 266401 (2018).
  - <sup>47</sup> Z. Zhan, Y. Zhang, P. Lv, H. Zhong, G. Yu, F. Guinea, J. A. Silva-Guillén, and S. Yuan, *Phys. Rev. B* **102**, 241106 (2020).
  - <sup>48</sup> L. Wang, E.-M. Shih, A. Ghiotto, L. Xian, D. A. Rhodes, C. Tan, M. Claassen, D. M. Kennes, Y. Bai, B. Kim, K. Watanabe, T. Taniguchi, X. Zhu, J. Hone, A. Rubio, A. N. Pasupathy, and C. R. Dean, *Nat. Mater.* **19**, 861 (2020).
  - <sup>49</sup> Z. Zhang, Y. Wang, K. Watanabe, T. Taniguchi, K. Ueno, E. Tutuc, and B. J. LeRoy, *Nat. Phys.* **16**, 1093 (2020).
  - <sup>50</sup> A. Ghiotto, E.-M. Shih, G. S. Pereira, D. A. Rhodes, B. Kim, J. Zang, A. J. Millis, K. Watanabe, T. Taniguchi, J. C. Hone, L. Wang, C. R. Dean, and A. N. Pasupathy, *Nature* **597**, 345 (2021).
  - <sup>51</sup> H. Li, U. Kumar, K. Sun, and S.-Z. Lin, *Phys. Rev. Res.* **3**, L032070 (2021).
  - <sup>52</sup> Y. Xu, K. Kang, K. Watanabe, T. Taniguchi, K. F. Mak,

- and J. Shan, *Nat. Nanotechnol.* **17**, 934 (2022).
- <sup>53</sup> D. Xiao, G.-B. Liu, W. Feng, X. Xu, and W. Yao, *Phys. Rev. Lett.* **108**, 196802 (2012).
- <sup>54</sup> G.-B. Liu, W.-Y. Shan, Y. Yao, W. Yao, and D. Xiao, *Phys. Rev. B* **88**, 085433 (2013).
- <sup>55</sup> P. J. Ledwith, E. Khalaf, Z. Zhu, S. Carr, E. Kaxiras, and A. Vishwanath, *arXiv preprint* (2021), 2111.11060.
- <sup>56</sup> S. Zhang, B. Xie, Q. Wu, J. Liu, and O. V. Yazyev, *Nano Lett.* **23**, 2921 (2023).
- <sup>57</sup> K. L. Seyler, P. Rivera, H. Yu, N. P. Wilson, E. L. Ray, D. G. Mandrus, J. Yan, W. Yao, and X. Xu, *Nature* **567**, 66 (2019).
- <sup>58</sup> C. Jin, E. C. Regan, A. Yan, M. Iqbal Bakti Utama, D. Wang, S. Zhao, Y. Qin, S. Yang, Z. Zheng, S. Shi, K. Watanabe, T. Taniguchi, S. Tongay, A. Zettl, and F. Wang, *Nature* **567**, 76 (2019).
- <sup>59</sup> K. Tran, G. Moody, F. Wu, X. Lu, J. Choi, K. Kim, A. Rai, D. A. Sanchez, J. Quan, A. Singh, J. Embrey, A. Zepeda, M. Campbell, T. Autry, T. Taniguchi, K. Watanabe, N. Lu, S. K. Banerjee, K. L. Silverman, S. Kim, E. Tutuc, L. Yang, A. H. MacDonald, and X. Li, *Nature* **567**, 71 (2019).
- <sup>60</sup> F. Wu, T. Lovorn, and A. H. MacDonald, *Phys. Rev. B* **97**, 035306 (2018).
- <sup>61</sup> F. Wu, T. Lovorn, and A. H. MacDonald, *Phys. Rev. Lett.* **118**, 147401 (2017).
- <sup>62</sup> Y. Xu, S. Liu, D. A. Rhodes, K. Watanabe, T. Taniguchi, J. Hone, V. Elser, K. F. Mak, and J. Shan, *Nature* **587**, 214 (2020).
- <sup>63</sup> K. Slagle and L. Fu, *Phys. Rev. B* **102**, 235423 (2020).
- <sup>64</sup> X. Huang, T. Wang, S. Miao, C. Wang, Z. Li, Z. Lian, T. Taniguchi, K. Watanabe, S. Okamoto, D. Xiao, S.-F. Shi, and Y.-T. Cui, *Nat. Phys.* **17**, 715 (2021).
- <sup>65</sup> T. Li, S. Jiang, B. Shen, Y. Zhang, L. Li, Z. Tao, T. Devakul, K. Watanabe, T. Taniguchi, L. Fu, J. Shan, and K. F. Mak, *Nature* **600**, 641 (2021).
- <sup>66</sup> E. C. Regan, D. Wang, C. Jin, M. I. Bakti Utama, B. Gao, X. Wei, S. Zhao, W. Zhao, Z. Zhang, K. Yumigeta, M. Blei, J. D. Carlström, K. Watanabe, T. Taniguchi, S. Tongay, M. Crommie, A. Zettl, and F. Wang, *Nature* **579**, 359 (2020).
- <sup>67</sup> D. M. Kennes, M. Claassen, L. Xian, A. Georges, A. J. Millis, J. Hone, C. R. Dean, D. Basov, A. N. Pasupathy, and A. Rubio, *Nat. Phys.* **17**, 155 (2021).
- <sup>68</sup> T. Li, S. Jiang, L. Li, Y. Zhang, K. Kang, J. Zhu, K. Watanabe, T. Taniguchi, D. Chowdhury, L. Fu, J. Shan, and K. F. Mak, *Nature* **597**, 350 (2021).
- <sup>69</sup> X. Wang, C. Xiao, H. Park, J. Zhu, C. Wang, T. Taniguchi, K. Watanabe, J. Yan, D. Xiao, D. R. Gamelin, W. Yao, and X. Xu, *Nature* **604**, 468 (2022).
- <sup>70</sup> M. Xie, H. Pan, F. Wu, and S. Das Sarma, *Phys. Rev. Lett.* **131**, 046402 (2023).
- <sup>71</sup> Y. Li, Z. Zhan, and S. Yuan, *Phys. Rev. B* **109**, 085118 (2024).
- <sup>72</sup> H. AlBuhairan and M. Vogl, *Phys. Rev. B* **108**, 155106 (2023).
- <sup>73</sup> H. Zheng, B. Wu, C.-T. Wang, S. Li, J. He, Z. Liu, J.-T. Wang, J.-a. Duan, and Y. Liu, *Nano Res.* **16**, 10573 (2023).
- <sup>74</sup> W. Liu, S. Luo, X. Qi, G. Guo, J. Li, H. Tang, X. Li, X. Huang, Z. Tang, and J. Zhong, *ACS Appl. Mater. Interfaces* **15**, 4724 (2023).
- <sup>75</sup> Y.-C. Leng, M.-L. Lin, Y. Zhou, J.-B. Wu, D. Meng, X. Cong, H. Li, and P.-H. Tan, *Nanoscale* **13**, 9732 (2021).
- <sup>76</sup> M. Liao, Z. Wei, L. Du, Q. Wang, J. Tang, H. Yu, F. Wu, J. Zhao, X. Xu, B. Han, K. Liu, P. Gao, T. Polcar, Z. Sun, D. Shi, R. Yang, and G. Zhang, *Nat. Commun.* **11**, 2153 (2020).
- <sup>77</sup> H. Zhong, Z. Su, and J. Kang, *Adv. Funct. Mater.* **34**, 2311814 (2024).
- <sup>78</sup> E. Tang, J.-W. Mei, and X.-G. Wen, *Phys. Rev. Lett.* **106**, 236802 (2011).
- <sup>79</sup> T. Neupert, L. Santos, C. Chamon, and C. Mudry, *Phys. Rev. Lett.* **106**, 236804 (2011).
- <sup>80</sup> D. Sheng, Z.-C. Gu, K. Sun, and L. Sheng, *Nat. Commun.* **2**, 389.
- <sup>81</sup> K. Sun, Z. Gu, H. Katsura, and S. Das Sarma, *Phys. Rev. Lett.* **106**, 236803 (2011).
- <sup>82</sup> N. Regnault and B. A. Bernevig, *Phys. Rev. X* **1**, 021014 (2011).
- <sup>83</sup> J. C. W. Song, P. Samutpraphoot, and L. S. Levitov, *Proc. Natl. Acad. Sci.* **112**, 10879 (2015).
- <sup>84</sup> Y.-H. Zhang, D. Mao, Y. Cao, P. Jarillo-Herrero, and T. Senthil, *Phys. Rev. B* **99**, 075127 (2019).
- <sup>85</sup> V. Crépel and L. Fu, *Phys. Rev. B* **107**, L201109 (2023).
- <sup>86</sup> N. Morales-Durán, J. Wang, G. R. Schleder, M. Angeli, Z. Zhu, E. Kaxiras, C. Repellin, and J. Cano, *Phys. Rev. Res.* **5**, L032022 (2023).
- <sup>87</sup> H. Pan, F. Wu, and S. Das Sarma, *Phys. Rev. Res.* **2**, 033087 (2020).
- <sup>88</sup> H. Pan, F. Wu, and S. Das Sarma, *Phys. Rev. B* **102**, 201104 (2020).
- <sup>89</sup> Y.-H. Zhang, D. N. Sheng, and A. Vishwanath, *Phys. Rev. Lett.* **127**, 247701 (2021).